PHYSICS

Nanoparticle-laden droplets of liquid crystals: Interactive morphogenesis and dynamic assembly

Yunfeng Li[1,2]*, Nancy Khuu[2], Elisabeth Prince[2], Moien Alizadehgiashi[2], Elizabeth Galati[2], Oleg D. Lavrentovich[3]*, Eugenia Kumacheva[2,4,5]*

Defects in liquid crystals serve as templates for nanoparticle (NP) organization; however, NP assembly in cholesteric (Ch) liquid crystals is only beginning to emerge. We show interactive morphogenesis of NP assemblies and a Ch liquid crystalline host formed by cellulose nanocrystals (CNCs), in which both the host and the guest experience marked changes in shape and structure as a function of concentration. At low NP loading, Ch-CNC droplets exhibit flat-ellipsoidal packing of Ch pseudolayers, while the NPs form a toroidal ring- or two cone–shaped assemblies at droplet poles. Increase in NP loading triggers reversible droplet transformation to gain a core-shell morphology with an isotropic core and a Ch shell, with NPs partitioning in the core and in disclinations. We show programmable assembly of droplets carrying magnetic NPs. This work offers a strategy for NP organization in Ch liquid crystals, thus broadening the spectrum of architectures of soft nanostructured materials.

INTRODUCTION

The ability to achieve precise organization of nanoparticles (NPs) in three-dimensional (3D) space is an important goal of research in the soft matter field. Template-based NP assembly offers a powerful and straightforward strategy for NP organization (1). A variety of templates, including nanotubes (2), block copolymers (3), viruses (4), and droplets (5), to name just a few, have been used to arrange NPs in structures that were predetermined by the template shape or structure. One of the promising approaches to NP assembly uses assembly in topological defects in liquid crystals (LCs). Defects represent distorted regions of the LC director, which cannot be transformed into a uniform state by continuous deformation (6). Defects have a core, in which the orientational LC order is different from that far away from the core (7). NPs added to an LC compartmentalize into the defect core to minimize the free energy of the system (8), thus assembling in chains (9, 10) and 2D lattices (11, 12).

Equilibrium states of confined volumes of LCs can contain defects that are stable because of the boundary conditions (13). In particular, spherical LC droplets have stable topological defects that are governed by the interplay of elastic and surface energies (14). Defects in nematic LC droplets have been used to position micrometer-size particles at two opposite droplet poles (8).

In cholesteric (Ch) LCs, the local director undergoes helicoidal twisting around a helical axis while being perpendicular to this axis. Continuous twist can be described as a 1D set of locally parallel "pseudolayers", with a well-defined pitch but no modulation of density (6). A pseudolayer is defined as a surface of a constant phase of the twist (6). Ch LCs confined in spherical droplets exhibit a series of defects (15–17). For example, when the Ch pitch P is larger than the droplet diameter D, the defects resemble those in the nematic phase; however,

when $P \ll D$, two new types of defects can be observed: a point defect formed by the radial field of the helicoidal axis (14, 18) and the disclination lines running in the radial direction from the core of the point defect to the droplet surface (14, 15, 19).

Recently, micrometer-size droplets of a colloidal Ch LC formed by a chiral nematic aqueous suspension of cellulose nanocrystals (CNCs) have been reported (20–23). In marked difference with droplets formed by thermotropic Ch molecules, ~100-μm-size Ch-CNC droplets with $P \ll D$ exhibited a large micrometer-size isotropic core and a Ch shell of concentrically packed Ch-CNC pseudolayers, which was pierced with disclinations. This core-shell morphology of lyotropic Ch LC is similar to the one obtained in the droplets of thermotropic LC (24, 25). Our group showed that polymer and inorganic NPs loaded in these core-shell droplets strongly compartmentalize into the isotropic core (23) and the radial disclinations (20). In other words, the Ch-CNC droplets with spherical packing of pseudolayers and radial disclinations served as efficient templates to control organization of guest NPs.

In the present work, we describe a previously unknown phenomenon in the self-assembly of NPs in Ch-CNC droplets, which can be called an "interactive morphogenesis". More specifically, we show that not only the liquid crystalline medium can control NP self-assembly, as reported previously for CNC-based LCs (20, 23) and for thermotropic LCs (26–39), but that the NPs can alter the morphology of the surrounding LC host. Furthermore, we show that the interactive morphogenesis of an LC host and magnetic NPs can be manipulated by applying an external magnetic field.

The present study was performed for relatively "small" Ch-CNC droplets with a diameter of ~20 μm. The CNCs in these droplets have tangential surface anchoring, with the director being parallel to the interface (23). In contrast to the "large" droplets studied previously (20, 23), small droplets contain only a few pseudolayers of Ch-CNCs, with $D/P \approx 3$, and exhibit a different morphology, that is, in the absence of NPs, these pseudolayers form a so-called hybrid flat-ellipsoidal structure, with the central pseudolayers being practically flat rather than spherical. Furthermore, the small Ch-CNC droplets contain defects that differ from those of the large droplets.

For 20-μm-diameter droplets, we found the phenomenon of interactive morphogenesis. The morphology and defects of the Ch-CNC droplets were changed by varying NP concentration. This effect

provided the capability to generate NP assemblies with programmable shapes. At a small volume fraction, ϕ_{NP}, NPs followed the template of the flat-ellipsoidal structure and formed two conical-shaped inclusions at the droplet poles. As ϕ_{NP} increased, the NP assemblies acquired the shape of a toroidal ring (TR). Further increase in ϕ_{NP} triggered complete reorganization of both the Ch-CNC and NP assemblies. The droplet morphology changes from the hybrid flat-ellipsoidal type to the core-shell type, with NP partitioned into the droplet core and radial disclinations. This interactive behavior is demonstrated for polymer (latex) and magnetic NPs. In the case of magnetic NPs, we expand control of their assembly to a new level by using a magnetic field. We show that the NPs can be shifted to one side of the droplets with a concomitant restructuring of the spherical Ch-CNC pseudolayers back to the flat-ellipsoidal configuration. Last, using the magnetic field to determine the location of magnetic NPs in the host Ch-CNC droplets, we achieve two different modes of droplet assembly, namely, linear and staggered chains.

RESULTS AND DISCUSSION

NP-free Ch-CNC droplets

Before NP loading in droplets, we studied the morphology of latex-free 20-μm-diameter Ch-CNC droplets. A suspension of negatively charged, rod-like CNCs with an average length and diameter of 176 ± 36 and 21 ± 6 nm, respectively (fig. S1A), and the CNC volume fraction of 0.046, was equilibrated for 21 days (no ultrasonication was applied to the suspension before the equilibration). Following the equilibration, the suspension phase-separated into an isotropic top phase and a Ch bottom phase with a pitch of ~6 μm and the CNC volume fraction of $\phi_0 = 4.8 \times 10^{-2}$. Later in the text, we refer to this Ch phase as to the Ch-CNC suspension. The Ch-CNC suspension was separated and emulsified in a microfluidic flow-focusing device (fig. S2) (40). Droplets with a diameter of ~20 μm and polydispersity of <10% were generated in fluorinated oil containing 0.5 weight % (wt %) of perfluoropolyether-co-poly(ethylene oxide-co-polypropylene oxide)-co-perfluoropolyether (denoted as F-oil). Following the emulsification, the droplets were equilibrated for 72 hours in a sealed fluid cell with a height of 400 μm.

We examined the texture of the droplets by polarized optical microscopy (POM). The textural appearance of the droplets depended on their orientation with respect to the optical axis of the microscope. We used the Cartesian coordinate (x, y, z) system, in which the z axis was aligned along the microscope optical axis, and the axes x and y were directed along the polarization directions of the polarizer and analyzer.

The Ch pseudolayers exhibited two types of packing (Fig. 1). Within a subsurface region (adjacent to the droplet surface), the pseudolayers formed a closed spherical shell with a thickness ~P. Further away from the surface, an ellipsoidal shell was formed. In Fig. 1A, the long axis of the ellipsoidal shell is labeled as the axis OO′. In the droplet interior, the Ch pseudolayers were flattened and elongated along the OO′ axis. We introduce an axis HH′ of the helicoidal director twist perpendicular to the pseudolayers in the droplet center (Fig. 1A). When the OO′ and HH′ axes were perpendicular to the z axis, the POM texture of the droplets revealed both the ellipsoidal subsurface packing and the flattened pseudolayers (Fig. 1, B and C). When the HH′ axis was parallel to the z axis, we observed the subsurface ellipsoidal packing, and the central part with flattened pseudolayers appeared as a solid ellipse (Fig. 1, D and E).
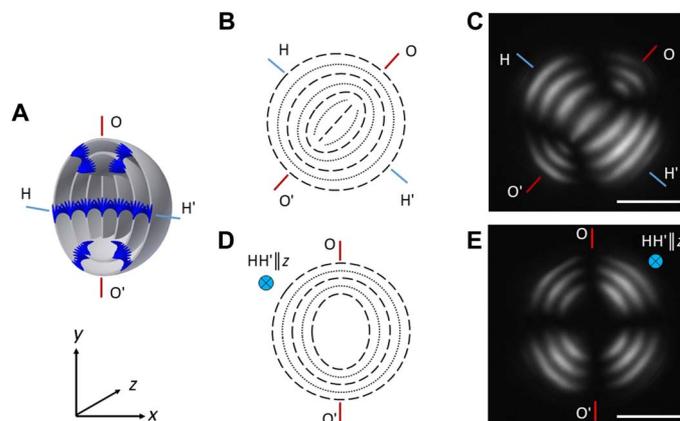

Fig. 1. NP-free Ch-CNC droplets. 3D (**A**) and cross-sectional schematics (**B** and **D**) and corresponding POM images (**C** and **E**) of the Ch-CNC droplets, with the OO′ and HH′ axes perpendicular to the z axis (B and C) and the HH′ axis parallel to the z axis (D and E). The light gray rings and dark blue rods in (A) represent the Ch-CNC pseudolayers and the CNCs, respectively. The dashed and dotted lines in (B) and (D) represent the CNC pseudolayers. In (C) and (E), $\phi_0 = 4.3 \times 10^{-2}$. Scale bars, 10 μm.

Organization of guest NPs in the Ch-CNC host droplets

We explored the organization of NPs in the Ch-CNC droplet host using 184-nm-diameter surfactant-free negatively charged latex NPs with electrokinetic potential of -41 ± 6 mV (measured in deionized water). A macroscopic Ch-CNC suspension was mixed with carboxylated fluorescein isothiocyanate (FITC)–labeled polystyrene NPs (fig. S1B) and emulsified in the microfluidic droplet generator (40). Figure 2 (A to J) shows the NP morphologies in the Ch-CNC droplets with $\phi_0 = 4.3 \times 10^{-2}$ and latex volume fraction ϕ_{NP} varying from 5.5×10^{-4} to 1.1×10^{-3} (a large population of droplets is shown in fig. S3). Figure 2 (left to right) shows the schematic, the fluorescence microscopy, the POM, and the merged images of the composite NP/Ch-CNC droplets. At $\phi_{NP} = 1.1 \times 10^{-4}$, the organization of NPs in the droplets resulted in a dominant bipolar (BP) morphology. The NPs enriched two opposite regions with a conical shape, which were located at the droplet poles in the transition region between the flattened and ellipsoidal Ch-CNC pseudolayers. These two regions were located at the OO′ axis (Fig. 2, A to E). The mean diameter of the NP inclusions was invariant at 6.2 ± 0.9 μm, when ϕ_{NP} increased from 1.1×10^{-4} to 5.5×10^{-4}.

With ϕ_{NP} increasing from 1.1×10^{-4} to 2.2×10^{-3} (Fig. 2, middle row), the NP assembly expanded by bridging the cone-like regions with a ring (Fig. 2, F to J), thus transforming the BP assembly into a TR structure with the two antipodal regions of conical shape ("handles"). The ring represented the region, in which the flattened pseudolayers in the droplet interior were perpendicular to the ellipsoidal pseudolayers in the shell. The ring's plane was perpendicular to the HH′ axis (Fig. 2, F to J). The TRs had an ellipsoidal shape with the long and short axes of 13.1 ± 1.3 and 11.8 ± 1.1 μm, respectively. The mean diameter of the handles increased from 4.1 ± 0.7 to 6.8 ± 1.3 μm for ϕ_{NP} increasing from 1.1×10^{-4} to 2.2×10^{-3}, respectively. The BP and TR assemblies of latex NPs did not change the flat-ellipsoidal geometry of the Ch-CNC host droplet, which was identical to that of the latex-free Ch-CNC droplets (shown in Fig. 1, C and E).

Interactive morphogenesis in NP-laden droplets

At higher latex NP loading of $\phi_{NP} \geq 5.5 \times 10^{-4}$, not only the Ch-CNC acted as a template for the NP assembly but also NPs affected the
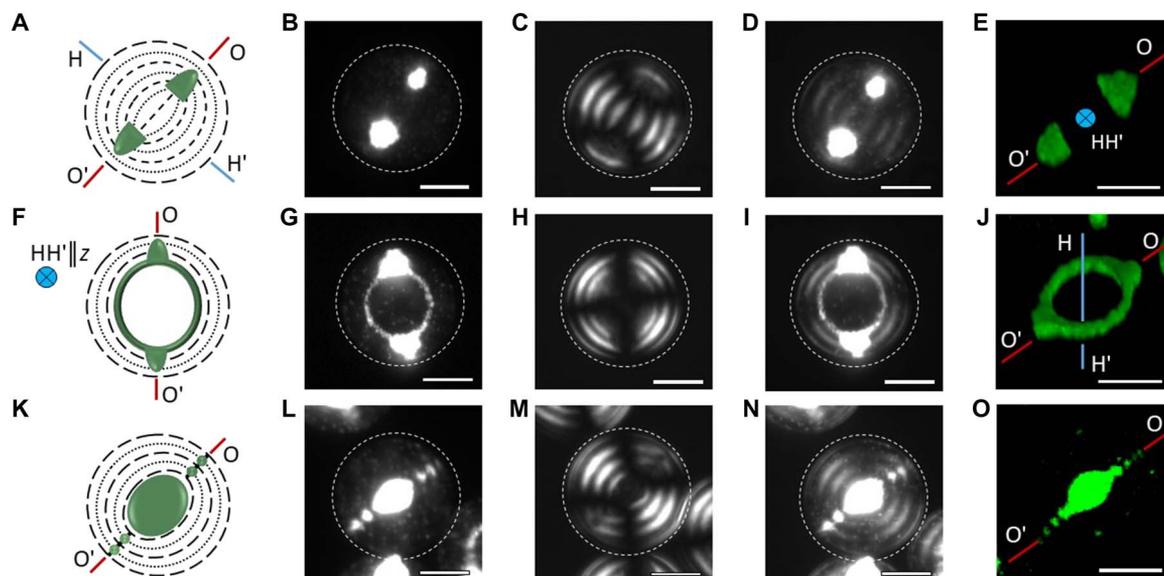
Fig. 2. Self-assembly of NPs in the Ch-CNC droplets. Schematics of the composite latex NP/Ch-CNC droplets with BP (**A**), TR (**F**), and core-shell disclination (CSD) (**K**) assemblies of the NPs. Representative fluorescence microscopy (**B, G,** and **L**), POM (**C, H,** and **M**), and merged (**D, I,** and **N**) images of the same NP/Ch-CNC droplet. (**E, J,** and **O**) 3D confocal fluorescence microscopy images of the NP assemblies with BP (E), TR (J), and CSD (O) structure. ϕ_{NP} is 5.5×10^{-4} in (B) to (E) and 1.1×10^{-3} in (G) to (O). $\phi_0 = 4.3 \times 10^{-2}$. Ch pseudolayers form flat-ellipsoidal structures in (A) to (J). Scale bars, 10 μm. Left: Orientation of the OO' and HH' axes (as in Fig. 1) and the corresponding notations for the orientation of the OO' and HH' axes with respect to the z axis (the optical axis of the microscope). The dashed and dotted lines and green deposits represent the CNC pseudolayers and latex NPs, respectively.

organization of Ch-CNC pseudolayers, that is, a new droplet morphology became prevalent. Thus, we observed interactive morphogenesis in the NP/Ch-CNC droplets: the Ch-CNC pseudolayer packing changed from the flat-ellipsoidal geometry to the core-shell structure, with a shell of concentrically packed Ch-CNC pseudolayers surrounding an isotropic core and disclination lines piercing the shell (Fig. 2, K to O). In these droplets, the latex NPs assembled in the ellipsoidal-shaped isotropic region in the droplet center and in the disclination lines (Fig. 2, K to O, and fig. S3A), thus exhibiting a core-shell disclination (CSD) morphology. Along the disclinations, the periodic 1D arrays of micrometer-large NP inclusions had the period equal to $P/2$. We note that the core-shell droplet morphology and the CSD assembly were previously observed only for large ~100-μm-diameter Ch-CNC droplets (*23*), in which the CNCs were in both the isotropic cores and the Ch shells (fig. S4). As ϕ_{NP} further increased to 1.19×10^{-2}, the minor and the major diameters of the central NP-rich core increased from 6.8 ± 2.0 to 13 ± 1.4 μm and from 9.8 ± 3.2 to 15.6 ± 1.3 μm, respectively, due to the stronger phase separation between the CNCs and the NPs with increasing latex NP content in the Ch-CNC suspension (fig. S5).

For a particular ϕ_{NP} and ϕ_0 combination, we observed the coexistence of NP/Ch-CNC droplets with different morphologies (Fig. 3A). For example, for $\phi_0 = 4.3 \times 10^{-2}$ and $\phi_{NP} = 1.1 \times 10^{-4}$, we observed a mixture of droplets with only BP and TR assemblies of NPs. When ϕ_{NP} was increased to 5.5×10^{-4}, in addition to BP and TR modes, ~30% of the assemblies had a CSD morphology. At $\phi_{NP} \geq 5.2 \times 10^{-3}$, we observed only the CSD organization of NPs. The state diagram plotted in the ϕ_{NP}-ϕ_0 coordinates in Fig. 3B shows the dependence of the NP assembly mode on the relationship between CNC and NP concentrations. At the low ϕ_{NP}/ϕ_0 ratios in the range of $0.013 < \phi_{NP}/\phi_0 < 0.018$, the BP, TR, and CSD morphologies coexisted, with the BP and TR assemblies being dominant. Increase of ϕ_{NP}/ϕ_0 resulted in a
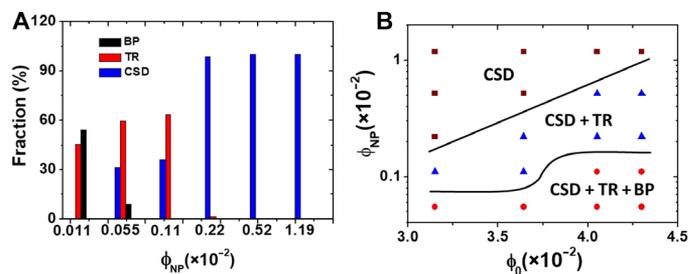

Fig. 3. Analysis of droplet morphologies. (**A**) Distribution of the populations of droplets with BP, TR, and CSD assemblies of NPs. For each sample, at least, 300 droplets were analyzed. $\phi_0 = 4.3 \times 10^{-2}$ in all the samples. (**B**) State diagram of the morphologies of NPs in the Ch-CNC droplets.

transition from the BP to the TR assembly. At $\phi_{NP} \geq 5.2 \times 10^{-3}$, only the CSD organization of NPs was observed in the entire range of ϕ_0 studied.

The sequence of transformations in NP and CNC organization with increasing ϕ_{NP} is shown schematically in Fig. 4, in which the regions of NP assemblies and the Ch-CNC pseudolayers are marked with green and gray colors, respectively. The label above each schematic specifies the corresponding Ch-CNC pseudolayer packing mode (red) and the NP assembly mode (blue). The NPs assembled in the regions with the strongest distortion of the director and the Ch order, in accordance with the mechanism demonstrated by Voloschenko *et al.* (*9*). The most unexpected feature was the NP-governed transition in the droplet morphology, that is, the change in the Ch-CNC pseudolayer packing from the flat-ellipsoidal to the core-shell (concentric) mode.

To explain the structural transitions observed in our work for the NP/Ch-CNC droplets, we consider an inclusion of a size R_P formed by the NPs in a Ch droplet. This inclusion will eliminate the orientational
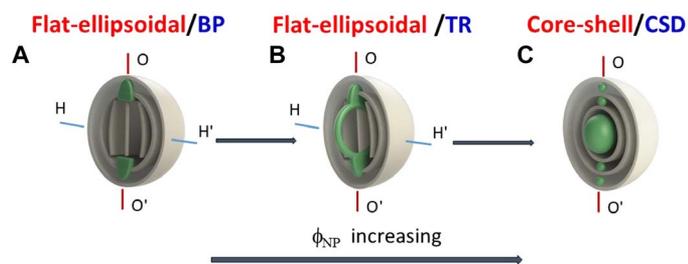
Fig. 4. Morphogenesis in the Ch-CNC host droplets and NP assemblies. (**A**) Flat-ellipsoidal/BP. (**B**) Flat-ellipsoidal/TR. (**C**) Core-shell/CSD. Gray planes represent the Ch-CNC pseudolayers. Green color marks latex NP assemblies. Labels above each schematic show the corresponding Ch-CNC packing mode (red font) and the NP assembly mode (blue font). To illustrate NP assembly, the schematics does not show the continuous twist of the CNCs.

order of the LC in a volume $V_p \sim R_p^3$. The resulting change in the free energy is [9]

$$\Delta E = -E_v + E_{si} + E_{sa} + E_{ind} \qquad (1)$$

where $E_v \sim KR_p^3/\xi^2$ is the elastic energy of the director deviations from the ideal Ch order in the volume V_p eliminated by the inclusion, K is the average Frank elastic constant (for the sake of simplicity, director distortion modes are not treated separately), and ξ is the characteristic length of the regions, in which the director deviates from the unperturbed Ch order (not to be confused with the nematic correlation length). E_{si} is the isotropic surface tension energy associated with the interface between the NPs and the Ch phase, E_{sa} is the anisotropic surface anchoring energy of the same interface, and E_{ind} is the energy of additional distortions induced by the inclusion. As follows from Eq. 1, the energetically preferred location of the inclusions would be the one that eliminates the LC region with the highest distortions. The corresponding energy gain $E_v \sim KR_p^3/\xi^2$ increases as the director gradients $\propto 1/\xi$ become stronger. In contrast, there is no energy gain, if the inclusion is placed in the uniform Ch structure, then $E_v \sim 0$.

Let us discuss first, how Eq. 1 can explain appearance of conical NP inclusions along the axis OO′. In these regions, the peripheral ellipsoidal pseudolayers meet the flattened pseudolayers in the interior in a perpendicular fashion (Fig. 4A and fig. S6). Besides the mismatch in the orientation of pseudolayers, these locations also correspond to singularities of the director field in each of the ellipsoidal Ch pseudolayers. A director field tangential to an ellipsoidal surface features topological defects of a total strength of 2 [6]. Figure S6 illustrates the director field in one of the Ch-CNC pseudolayers as red lines encircling the cores of the two defects of charge +1, each, with the cores aligned along the OO′ axis (shown as the green cones in Fig. 4A). We associate these cores along the OO′ axis with the regions in which the NPs accumulate first, thus forming the BP assemblies with two compact cone-like inclusions of a typical size $R_p \sim P$. The main term in Eq. 1 that describes conical NP assemblies along the OO′ axis (Fig. 4A) is the elastic gain term, $E_v \sim KR_p^3/\xi^2$, because ξ achieves its smallest value, on the order of P, in the regions of mismatch of pseudolayers orientation and director singularities; while in the rest of the system, ξ is larger. The term E_{ind} is less significant, as the overall configuration of Ch pseudolayers is preserved. The surface terms E_{si} and E_{sa} are also not significant as they do not considerably change when the NP inclusion is moved within the Ch droplet. The size of these two conical assemblies is limited from above, as their enlargement above the typical size $\sim P$ would increase

the surface energy terms in Eq. 1, since the interfacial area grows as the square of the inclusion's size and cause additional deformations in the surrounding Ch pseudolayers, thus increasing E_{ind}.

As follows from the experiments (Fig. 2, G to J), when ϕ_{NP} increases to be in the range of 5.5×10^{-4} to 1.1×10^{-3}, the NPs accumulate not only in the conical centers but also along the rest of the TR, where the flattened and ellipsoidal Ch pseudolayers meet each other (fig. S6). To understand this feature using Eq. 1, the shape of the NP assembly can be modeled as a solid torus (the term "solid" is used in the topological sense to stress that the interior of the torus is filled with NPs; however, physically, these interiors are soft). A solid torus can be characterized by two radii: the radius of a small disk R_{small} (which measures how "thick" the torus is) and the large radius R_{large} (which specifies how "wide" the torus is). The gain in the elastic energy caused by the assembly of NPs in the torus is on the order of $E_v^{ring} \sim KR_{small}L_{ring}/\xi$, where $R_{small} \sim \xi \sim P$, $L_{ring} = 2\pi R_{large}$, and L_{ring} is the length of the torus along its circular axis. Thus, Eq. 1 suggests that the formation of conical and ring assemblies of NPs is driven by the gain in the elastic energy that occurs whenever a strongly distorted region of an LC is replaced by a foreign material, as previously reported for inclusions in thermotropic LCs [9].

Upon further addition of NPs and a transformation from the flat-ellipsoidal to the core-shell droplet morphology, the transformation of the TR assembly of NPs into the CSD assembly is associated with the contributions of the E_{si}, E_{sa}, and E_{ind} terms in Eq. 1. The collapse of the ring into an ellipsoidal core reduces the Ch-CNC/NP interface and thus decreases the isotropic surface tension energy E_{si}. Moreover, one also expects a decrease in the anchoring energy E_{sa} upon such a transformation, because in the CSD assembly, the director is tangential to the Ch-CNC/NP interface, which is the preferred CNC alignment [20, 23]. In the cases of BP and TR assemblies, the tangential surface alignment of the director is difficult to achieve, since at least, some of the Ch-CNC pseudolayers cross the assemblies in a perpendicular fashion (fig. S6). The core-shell droplet morphology implies the presence of disclinations in the Ch shell. These disclinations attract NPs and form periodic linear arrays of NPs along their cores, as observed in Figs. 2 (L to O) and 4C, in agreement with the previous work [20].

Loading of magnetic NPs in guest Ch-CNC droplets
To expand the functionality of the NP-laden droplets and explore interactive morphogenesis of NP guests and the Ch-CNC host in greater details, we introduced ~100-nm-diameter superparamagnetic Fe_3O_4 NPs stabilized with polyacrylic acid (fig. S7) in the Ch-CNC phase and generated composite droplets by the microfluidic emulsification. After 3-day equilibration at $\phi_{NP} = 9.7 \times 10^{-4}$, the TR assembly (Fig. 5, A-A″ and B-B″) of the NPs was dominant (60.5%), with 16.6 and 22.9% of the NPs exhibiting the BP and CSD assemblies, respectively. Depending on the viewing direction, the TR assembly in the droplets appeared either as an elongated cylinder (when OO and HH′ were both perpendicular to the z axis) (Fig. 5A′) or as an elliptical ring with handles (HH′∥z axis), as shown in Fig. 5B′. At a higher NP loading of $\phi_{NP} = 1.9 \times 10^{-3}$, 100% of the droplets exhibited a core-shell morphology (Fig. 5, C to C″ and fig. S8). Since this behavior was similar for the latex and Fe_3O_4 NPs, we speculate that interactive morphogenesis is general for negatively charged NPs with dimensions of 100 to 200 nm, which are compartmentalized in the Ch-CNC droplets.

Subsequently, we explored the effect of the magnetic field on the Ch-CNC droplets laden with Fe_3O_4 NPs. Under the action of the magnetic field, we observed two phenomena that depended on the field strength and the time of its application. First, within the droplets, the
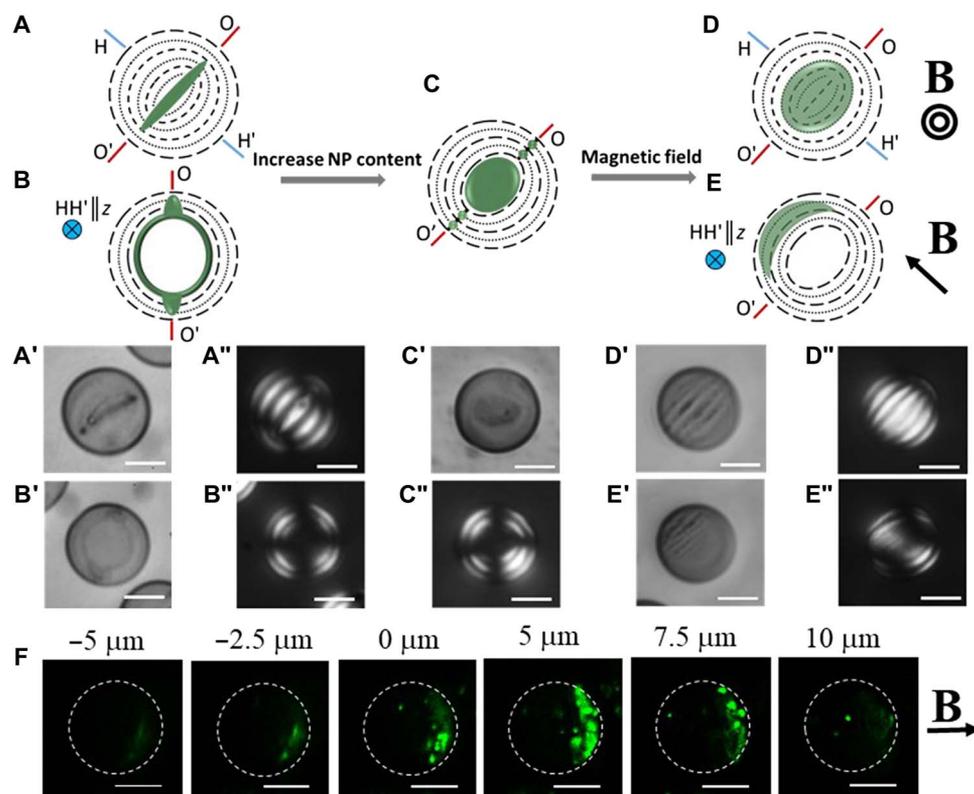
Fig. 5. Interactive morphogenesis in Ch-CNC droplets laden with magnetic NPs. Representative schematic (**A** to **C**) and corresponding bright-field (**A′**, **B′**, and **C′**) and POM (**A″**, **B″**, and **C″**) images of the Ch-CNC droplets loaded with Fe_3O_4 NPs with TR (A′, A″ and B′, B″) and CSD (C′ and C″) assemblies. $\phi_{NP} = 9.7 \times 10^{-4}$ and 1.9×10^{-3} in (A′ to B″) and in (C′) and (C″), respectively. No magnetic field is applied. Representative schematic (**D** and **E**) and corresponding bright-field (**D′** and **E′**) and POM (**D″** and **E″**) images of the Ch-CNC droplets loaded with Fe_3O_4 NPs at $\phi_{NP} = 9.7 \times 10^{-4}$ and exposed to a 0.35-T magnet for 3 days. $\phi_0 = 4.3 \times 10^{-2}$ in all the samples. Scale bars, 10 μm. Top row shows the orientation of the OO′ and HH′ axes (as in Fig. 1) and the corresponding notations for the orientation of the OO′ and HH′ axes with respect to the z axis (the optical axis of the microscope). Dashed lines and dotted lines and green deposits represent the CNC pseudolayers and NPs, respectively. (**F**) Z-stack fluorescence microscopy images of the Ch-CNC droplets shown in (D) and (E). The 0-μm position corresponds to the central plane of the droplets, and the images were taken on the top (negative values) to the bottom (positive values) of this plane. $\phi_{NP} = 9.7 \times 10^{-4}$ and $\phi_0 = 4.3 \times 10^{-2}$ in all the samples. Scale bars, 10 μm.

Fe_3O_4 NPs moved from the BR, TR, and CSD defects to the droplet side adjacent to the magnet. Because of the high viscosity of the Ch-CNC suspension, this motion was slow: Under 0.35-T field, the accumulation of NPs on the droplet side facing the magnet took ~3 days. Second, the NP-laden droplets moved toward to the magnet with the average velocity of ~400 μm/s.

A permanent magnetic field (0.35 T) was applied for 3 days to the emulsion of Ch-CNC droplets laden with Fe_3O_4 NPs at $\phi_{NP} = 9.7 \times 10^{-4}$. Under these conditions, the droplets moved to the side of the fluid cell that was adjacent to the magnet and formed a close-packed 3D array (fig. S9). Within the droplets, the NPs transferred to the droplet side (Fig. 5, D to D″ and E to E″) facing the magnet, thus assembling at a single droplet pole (Fig. 5F and fig. S10). Within this region, the NPs were localized in curved layers in the droplet subsurface, as shown in Fig. 5D′ (OO and HH′⊥z axis) and E′ (HH′∥z). After removing the magnetic field, within 21 days, this NP assembly did not relax to the BP or TR type.

Following magnetically triggered NP transfer to the single pole of the droplet, the core-shell morphology of the Ch-CNC host (Fig. 5, C′ and C″) changed to the flat-ellipsoidal morphology (Fig. 5, D″ and E″), thus reversing interactive morphogenesis. We note that the textural appearance of the host Ch-CNC droplets and assemblies of magnetic NPs depended on their orientation with respect to the optical

axis of the microscope. When the OO′ and HH′ axes were perpendicular to the z axis (Fig. 5D), the POM texture of the droplets revealed both the ellipsoidal subsurface packing and the flattened pseudolayers, with the layers of magnetic NP arrays covering the subsurface layer, thus forming a magnetic NP pole (Fig. 5, D′ and D″). When the HH′ axis was parallel to the z axis, the subsurface ellipsoidal packing was observed, and the ellipsoidal central part with flattened pseudolayers was observed, with magnetic NP layers decorating the subsurface layer on the droplet side (Fig. 5, E′ and E″).

Dynamic assembly of Ch-CNC droplets laden with magnetic NPs

To study the dynamic assembly of the Ch-CNC droplets with different locations of magnetic Fe_3O_4 NPs at $\phi_{NP} = 9.7 \times 10^{-4}$, a sealed fluid cell with the emulsion of droplets was introduced in the magnetic field, which was generated by two permanent magnets (0.35 T) separated with a distance of ~5.5 cm. Within 10 min, we observed two types of magnetically induced assembly of the NP/Ch-CNC droplets, namely, their organization in linear and staggered chains. During the course of droplet assembly, no noticeable motion of magnetic NPs within the droplets was observed.

We first explored the assembly of NP/Ch-CNC droplets with BP, TR, and CSD morphologies (shown in Fig. 5, A to C). Without the

magnetic field, these Ch-CNC droplets were randomly dispersed in the fluid cell. Under a magnetic field, the Fe_3O_4 NPs in the droplets were magnetized, and the major axis of the BP, TR, and CSD assemblies became parallel to the direction of the magnetic field, thus resulting in the movement of the droplets toward to the magnet. During this movement, because of the attraction between the magnetic dipoles of the droplets, they formed short linear chains. As individual droplets and droplet chains were approaching the magnet, the emulsion became more concentrated, and the length of the linear chains gradually increased. In the chains, within 10 to 20 min, magnetic NP assemblies retained their BP, TR, and CSD morphologies in the neighboring droplets and were facing each other in the direction parallel to the long axis of the chains (Fig. 6, B and C, and fig. S11, A and B). We observed no noticeable change in the texture of the Ch-CNC droplets. When the magnetic field was removed, the chains lost their integrity, and the droplets were dispersed in the F-oil in ~5 min.

We explored the second type of dynamic assembly for the Ch-CNC droplets laden with Fe_3O_4 NPs localized at the single droplet pole (Fig. 5, D′ to E″). Because of the attraction of magnetic dipoles, the droplets interacted with each other with the formation of staggered chains moving toward to the magnet. Within the chains, the magnetic NP assemblies of the adjacent droplets faced each other but pointed in alternating directions (Fig. 6, E and F). The NP assemblies were oriented parallel to the direction of the magnetic field, in contrast to their perpendicular orientation in individual droplets (shown in Fig 5, D to F), since parallel orientation along the field direction provided the strongest attractive interactions between the NP assemblies in droplet chains, in agreement with earlier observations for iron oxide–capped Janus particles (41). The organization of magnetic NPs and the texture of Ch-CNC droplets remained constant during the droplet assembly process. While approaching the magnet, short staggered droplet chains attracted individual droplets to form longer assemblies (fig. S11, C and D). When the magnetic field was removed, the chains of Ch-CNC droplets disassembled within 5 min.

We note that the magnetically driven assembly of the Ch-CNC droplets laden with Fe_3O_4 NPs (shown in Fig. 6) has features that make it distinct from the assembly of solid particles with magnetic patches (41–44). The soft nature of the Ch-CNC host and the transformations of the topological defects (NP templates) render the ability to deform and manipulate NP-laden droplets by magnetic forces, thus paving the way for the preparation of complex functional soft materials and devices (45–47). The ease of loading NPs in these droplets opens the door

for new approaches to dynamic reactors (47) and patchy droplets with complex shapes (47). In addition, the inherent properties of an LC in the droplets may lead to assemblies with new collective functions, such as cross-communications (48).

CONCLUSIONS
In conclusion, we demonstrated interactive morphogenesis of NP assemblies and Ch liquid crystalline order of CNCs within spherical microdroplets. The initial, NP-free Ch droplets showed a flat-ellipsoidal packing of Ch pseudolayers. At the relatively low NP loading, this Ch packing guided the assembly of the guest NPs to the regions of the highest distortions of the orientational order, thereby producing cone-shaped NP assemblies at the droplet poles and, at a somewhat higher NP loading, TR NP assembly. Further increase in NP loading resulted in a marked reconstruction of the morphology of the Ch-CNC host itself: The flat-ellipsoidal packing of the Ch-CNC pseudolayers changed to the concentric spherical Ch packing. The NPs in these concentric structures partitioned into the droplet core and in the disclinations in the Ch shell. The interactive morphogenesis was generic for both polymeric and inorganic magnetic NPs. We transformed the core-shell morphology of the Ch-CNC host back to the planar-ellipsoidal morphology by magnetically triggered NP transfer to a single droplet pole, thus reversing interactive morphogenesis.

Partitioning of NPs into the regions with strongly distorted director is reminiscent of a similar effect (9, 31, 36–39) for thermotropic LCs, in which the defect cores served as locations that attract non-LC inclusions. In these works, the LC structure controlled the guest NP assembly; however, it did not significantly change as a result of this assembly. More generally, reports published, so far, indicate that various liquid crystalline templates, both thermotropic (9–12, 36–38, 49) and lyotropic (20, 23) that were used for colloidal assembly at the nanoscale and microscale, are relatively insensitive structures: They determine the shape of assemblies but do not change significantly in this process. Our study presents an example of interactive morphogenesis, in which the NP assembly markedly modifies the liquid crystalline host as the content of NPs in the system increases. We are not aware of any report on a similar effect in the thermotropic LCs. One explanation might invoke the difference in the building units (molecules versus nanocrystals). However, Eq. 1 suggests that there are no fundamental reasons to prohibit such an interactive morphogenesis in the thermotropic LCs loaded with NPs; whether it could be observed or not would
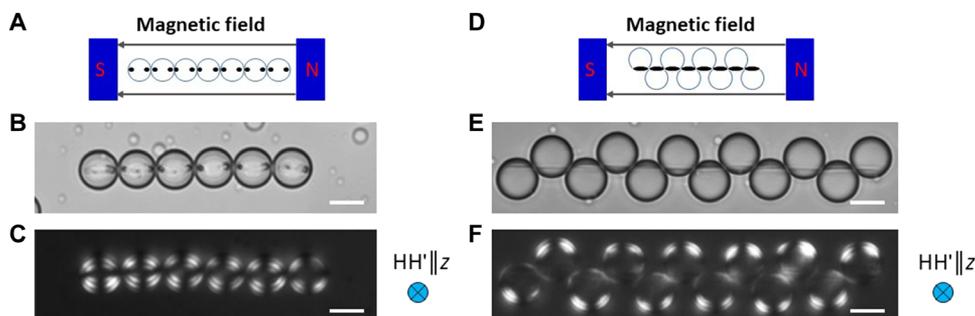
Fig. 6. Different models of assembly of Ch-CNC droplets laden with Fe_3O_4 NPs under magnetic field. (**A** to **C**) Schematic and corresponding bright-field (B) and POM (C) images of chains formed by Ch-CNC droplets with BP and TR assemblies of NPs. Droplets with the CSD assembly of NPs showed similar assembly in linear chains and are not shown. (**D** to **F**) Schematic and corresponding bright-field (E) and POM (F) images of staggered chains formed by Ch-CNC droplets loaded with magnetic NPs that were localized in the subsurface layer on one side of the droplets. $\phi_{NP} = 9.7 \times 10^{-4}$ and $\phi_0 = 4.3 \times 10^{-2}$. Scale bars, 20 μm. HH′ axis was parallel to the z axis in (C and F).

depend on the specific material properties, such as elastic constants, interfacial tension, and surface anchoring.

We also demonstrate that the soft nature of the Ch-CNC host enables magnetic field manipulation of the NP assemblies and transfer of the magnetic NPs to different locations in the droplet, yielding two different modes of droplet assembly, namely, linear and staggered chains. The interplay between the structure of the host Ch-CNC droplet and the NP organization represents a new approach to programmable NP assemblies with different compositions, shapes, and dimensions. The utilization of the Ch-CNC lyotropic LC expands the range of architectures and compositions realized in soft nanostructured materials.

MATERIALS AND METHODS
Materials
An aqueous suspension of CNCs (11.8 wt %) was supplied by the Process Development Center of the University of Maine. The CNCs (fig. S1A) with an average length L and diameter D of 176 ± 36 and 21 ± 6 nm, respectively, were obtained by acid hydrolysis of wood pulp. The polydispersity of the CNC diameter and length were 20 and 29%, respectively, determined by the analysis of their transmission electron microscopy (TEM) images. To suppress CNC aggregation, a dilute 0.01 wt % suspension of CNCs was drop-cast on a TEM grid that was treated by oxygen plasma for 10 s. The TEM images were obtained using a Hitachi HT7700 microscope at 85 kV. In fig.S1A, several individual CNCs are marked with white boxes. The size measurement positions on an individual CNC is shown in inset of fig.S1A. The CNC length and the diameter were characterized by measuring the dimensions of 100 CNCs using the ImageJ software. The electrokinetic potential of the CNCs was −47 ± 9 mV.

The FITC-labeled polystyrene latex NPs (184 nm, Fluoresbrite YG Carboxylate Microspheres) were purchased from Polysciences. The polydispersity and electrokinetic potential of the NPs was 3.6% and −41 ± 6 mV, respectively. The magnetite NPs were supplied by Chemicell. The size of the magnetic NPs and the electrokinetic potential of the NPs were 100 nm and −30 ± 6 mV, respectively, in water measured by Zetasizer (Malvern). The volume fraction of magnetic NPs was calculated using the density of magnetic NPs of 5.18 g/cm³. Fluorinated oil HFE-7500 3M Novec was purchased from MG Chemicals. The perfluoropolyether-co-poly(ethylene oxide-co-polypropylene oxide)-co-perfluoropolyether copolymer [PFPE-P(EO-PO)-PFPE] was synthesized, as described elsewhere, and used as a surfactant (50). The photoresist SU-8 was supplied by MicroChem. Poly(dimethylsiloxane) (PDMS; Sylgard 184) was purchased from Dow Corning. All other chemicals were purchased from Aldrich Canada.

A CNC suspension (10 ml) with CNC concentration varying from 5 to 7 wt % (or volume fraction from 3.3×10^{-2} to 4.6×10^{-2}) was introduced into a glass vial with a diameter of 2.5 cm. The volume fraction of CNCs was calculated using the density of CNCs of 1.566 g/cm³ (51). The volume of an individual CNC, v_{CNC} was calculated as $v_{CNC} = \pi \left(\frac{D}{2}\right)^2 L$, by assuming a cylindrical shape of CNCs. Following equilibration for 21 days, the CNC suspension was phase-separated into a top isotropic phase and a bottom Ch phase. Following phase separation, the Ch phase was removed from the vial with a syringe using a 22-gauge needle.

Fabrication of microfluidic devices
The flow-focusing microfluidic droplet generator was fabricated in PDMS. Photoresist SU-8 masters were prepared by photolithography on the silicon wafers. After fabrication, the devices were maintained in an oven at 140°C for 12 hours to increase the hydrophobicity of the microchannel surface. The dimensions of the microfluidic device are shown in fig. S2.

Preparation of Ch-CNC droplets loaded with latex NPs and magnetic NPs
A mixture of the Ch-CNC suspension and latex NPs was emulsified in the flow-focusing microfluidic droplet generator (fig.S2) (40) using a syringe pump (Harvard Apparatus PHD 2000 Syringe Pump, USA). A mixture of 50 μl of NP dispersion with NP concentration from 1.1×10^{-3} to 1.19×10^{-1} and 450 μl of the Ch-CNC phase was prepared by shaking at 50 Hz for 2 min at 25°C in a vortex mixer and immediately supplied to the microfluidic droplet generator as a droplet phase. Fluorinated oil HFE-7500 mixed with 0.5 wt % of the copolymer surfactant (denoted as F-oil) was supplied to the microfluidic device as a continuous phase by using the second syringe pump (PHD 2000 Harvard Apparatus, USA). The flow rate of F-oil and the Ch-CNC/NP mixture were 0.2 and 0.02 ml/hour, respectively. The droplets were collected in a 2-ml vial and transferred into a cell consisting of two parallel glass slides separated with a 400-μm-thick spacer. The cell was sealed with epoxy glue, and the droplets were equilibrated for 3 days.

The procedure of the generation of the NP-free Ch-CNC droplets was similar to the protocol of the preparation of the Ch-CNC/NP droplets. Deionized water (50 μl) was added to 450 μl of the Ch-CNC phase to achieve the same concentration of CNCs in both cases. The suspension was mixed at 50 Hz for 2 min at 25°C in a vortex mixer and, subsequently, emulsified in the microfluidic device.

The method of preparation of Ch-CNC droplets loaded with magnetic NPs is similar to the procedure of generation of the Ch-CNC droplets loaded with latex NPs. Instead of using latex NPs, a mixture of 50 μl of magnetic NP dispersion with NP volume fraction from 9.7×10^{-3} to 1.9×10^{-2} and 450 μl of the Ch-CNC phase was prepared by shaking at 50 Hz for 2 min at 25°C in a vortex mixer and immediately supplied to the microfluidic droplet generator as a droplet phase.

Phase separation in the macroscopic mixed suspension of CNCs and latex NPs
A mixture of the Ch-CNC phase (2.7 ml, $\phi_0 = 4.8 \times 10^{-2}$) and the dispersion of 184-nm FITC-labeled latex NPs (300 μl, ϕ_{NP} is from 0 to 1.19×10^{-1}) was shaken at 50 Hz for 3 min at 25°C in a vortex mixer. The volume fractions of the latex NPs and CNCs in the mixed suspension were 0 to 1.19×10^{-2} and 4.3×10^{-2}, respectively. A mixture (3 ml) of the Ch-CNC phase and latex NPs was introduced into a glass vial and equilibrated for 35 days. Following equilibration for 35 days, the suspension was phase-separated into a top latex-rich isotropic phase and a bottom CNC-rich Ch phase (fig. S5). The images of these phases were acquired using a Nikon D7200 camera. The heights of the two phases were determined by analyzing the images using the software ImageJ. The SD in determining the heights of the isotropic and Ch phases did not exceed 0.1 mm.

Characterization of droplets
The bright-field, POM, and fluorescence microscopy images were taken on an optical microscope (Olympus BX51) in the transmission mode. The diameters of the droplets and the pitch of the Ch phase in the droplets were measured using the software ImageJ. The Z-stack fluorescence images of the Ch-CNC droplets loaded with FITC-labeled

latex NPs were taken by a Zeiss LSM 710 confocal microscope. The dimensions of the NP assemblies were characterized by measuring their geometric mean diameter, which was calculated by measuring two orthogonal diameters, and finding the square root of their product.

SUPPLEMENTARY MATERIALS

Supplementary material for this article is available at http://advances.sciencemag.org/cgi/content/full/5/7/eaav1035/DC1

Fig. S1. TEM characterization of CNCs and latex NPs.
Fig. S2. Optical microscopy images of the Ch-CNC/NP droplets generated in the MF flow-focusing droplet generator.
Fig. S3. Characterization of the Ch-CNC droplets loaded with latex NPs.
Fig. S4. Characterization of the NP-free Ch-CNC droplets.
Fig. S5. Phase separation of mixtures of Ch-CNC suspension and latex NPs.
Fig. S6. Schematic of the flat-ellipsoidal droplet structure of the Ch-CNC droplets.
Fig. S7. TEM images of magnetic Fe_3O_4 NPs.
Fig. S8. Characterization of the Ch-CNC droplets loaded with magnetic NPs.
Fig. S9. 3D assemblies of the Ch-CNC droplets loaded with Fe_3O_4 NPs.
Fig. S10. Characterization of the Ch-CNC droplets with the layers of magnetic NP.
Fig. S11. Two models of assembly of the Ch-CNC droplets laden with Fe_3O_4 NPs under the magnetic field.

REFERENCES AND NOTES

1. Z. Nie, A. Petukhova, E. Kumacheva, Properties and emerging applications of self-assembled structures made from inorganic nanoparticles. *Nat. Nanotechnol.* **5**, 15–25 (2010).
2. M. A. Correa-Duarte, J. Pérez-Juste, A. Sánchez-Iglesias, M. Giersig, L. M. Liz-Marzán, Aligning Au nanorods by using carbon nanotubes as templates. *Angew. Chem. Int. Ed.* **44**, 4375–4378 (2005).
3. Q. Zhang, S. Gupta, T. Emrick, T. P. Russell, Surface-functionalized CdSe nanorods for assembly in diblock copolymer templates. *J. Am. Chem. Soc.* **128**, 3898–3899 (2006).
4. E. Dujardin, C. Peet, G. Stubbs, J. N. Culver, S. Mann, Organization of metallic nanoparticles using tobacco mosaic virus templates. *Nano Lett.* **3**, 413–417 (2003).
5. J. I. Park, A. Kumachev, A. I. Abdelrahman, B. P. Binks, H. A. Stone, A microfluidic approach to chemically driven assembly of colloidal particles at gas-liquid interfaces. *Angew. Chem. Int. Ed.* **48**, 5300–5304 (2009).
6. M. Kleman, O. D. Lavrentovich, *Soft Matter Physics: An Introduction* (Springer, 2003).
7. S. Zhou, S. V. Shiyanovskii, H.-S. Park, O. D. Lavrentovich, Fine structure of the topological defect cores studied for disclinations in lyotropic chromonic liquid crystals. *Nat. Commun.* **8**, 14974 (2017).
8. J. K. Whitmer, X. Wang, F. Mondiot, D. S. Miller, N. L. Abbott, J. J. de Pablo, Nematic-field-driven positioning of particles in liquid crystal droplets. *Phys. Rev. Lett.* **111**, 227801 (2013).
9. D. Voloschenko, O. P. Pishnyak, S. V. Shiyanovskii, O. D. Lavrentovich, Effect of director distortions on morphologies of phase separation in liquid crystals. *Phys. Rev. E* **65**, 060701 (2002).
10. D. Coursault, J. Grand, B. Zappone, H. Ayeb, G. Lévi, N. Félidj, E. Lacaze, Linear self-assembly of nanoparticles within liquid crystal defect arrays. *Adv. Mater.* **24**, 1461–1465 (2012).
11. I. Muševič, M. Škarabot, U. Tkalec, M. Ravnik, S. Žumer, Two-dimensional nematic colloidal crystals self-assembled by topological defects. *Science* **313**, 954–958 (2006).
12. D. K. Yoon, M. C. Choi, Y. H. Kim, M. W. Kim, O. D. Lavrentovich, H.-T. Jung, Internal structure visualization and lithographic use of periodic toroidal holes in liquid crystals. *Nat. Mater.* **6**, 866–870 (2007).
13. O. D. Lavrentovich, Topological defects in dispersed words and worlds around liquid crystals, or liquid crystal drops. *Liq. Cryst.* **24**, 117–126 (1998).
14. M. V. Kurik, O. D. Lavrentovich, Topological defects of cholesteric liquid crystals for volumes with spherical shape. *Mol. Cryst. Liq. Cryst.* **72**, 239–246 (2007).
15. D. Seč, T. Porenta, M. Ravnik, S. Žumer, Geometrical frustration of chiral ordering in cholesteric droplets. *Soft Matter* **8**, 11982–11988 (2012).
16. T. Orlova, S. J. Aßhoff, T. Yamaguchi, N. Katsonis, E. Brasselet, Creation and manipulation of topological states in chiral nematic microspheres. *Nat. Commun.* **6**, 7603 (2015).
17. Y. Zhou, E. Bukusoglu, J. A. Martínez-González, M. Rahimi, T. F. Roberts, R. Zhang, X. Wang, N. L. Abbott, J. J. de Pablo, Structural Transitions in Cholesteric Liquid Crystal Droplets. *ACS Nano* **10**, 6484–6490 (2016).
18. C. Robinson, Liquid-crystalline structures in solutions of a polypeptide. *Trans. Faraday Soc.* **52**, 571–592 (1956).
19. M. V. Kurik, O. D. Lavrentovich, Negative-positive monopole transitions in cholesteric liquid crystals. *J. Exp. Theor. Phys. Lett.* **35**, 444–447 (1982).
20. Y. Li, E. Prince, S. Cho, A. Salari, Y. Mosaddeghian Golestani, O. D. Lavrentovich, E. Kumacheva, Periodic assembly of nanoparticle arrays in disclinations of cholesteric liquid crystals. *Proc. Natl. Acad. Sci. U.S.A.* **114**, 2137–2142 (2017).
21. R. M. Parker, B. Frka-Petesic, G. Guidetti, G. Kamita, G. Consani, C. Abell, S. Vignolini, Hierarchical Self-Assembly of Cellulose Nanocrystals in a Confined Geometry. *ACS Nano* **10**, 8443–8449 (2016).
22. P.-X. Wang, W. Y. Hamad, M. J. Maclachlan, Polymer and mesoporous silica microspheres with chiral nematic order from cellulose nanocrystals. *Angew. Chem. Int. Ed.* **55**, 12460–12464 (2016).
23. Y. Li, J. J.-Y. Suen, E. Prince, E. M. Larin, A. Klinkova, H. Thérien-Aubin, S. Zhu, B. Yang, A. S. Helmy, O. D. Lavrentovich, E. Kumacheva, Colloidal cholesteric liquid crystal in spherical confinement. *Nat. Commun.* **7**, 12520 (2016).
24. A. Darmon, M. Benzaquen, D. Seč, S. Čopar, O. Dauchot, T. Lopez-Leon, Waltzing route toward double-helix formation in cholesteric shells. *Proc. Natl. Acad. Sci. U.S.A.* **113**, 9469–9474 (2016).
25. A. Darmon, M. Benzaquen, S. Čopar, O. Dauchot, T. Lopez-Leon, Topological defects in cholesteric liquid crystal shells. *Soft Matter* **12**, 9280–9288 (2016).
26. M. Mitov, C. Portet, C. Bourgerette, E. Snoeck, M. Verelst, Long-range structuring of nanoparticles by mimicry of a cholesteric liquid crystal. *Nat. Mater.* **1**, 229–231 (2002).
27. D. Voloschenko, O. D. Lavrentovich, Light-induced director-controlled microassembly of dye molecules from a liquid crystal matrix. *J. Appl. Phys.* **86**, 4843–4846 (1999).
28. M. Škarabot, M. Ravnik, S. Žumer, U. Tkalec, I. Poberaj, D. Babič, I. Muševič, Hierarchical self-assembly of nematic colloidal superstructures. *Phys. Rev. E Stat. Nonlin. Soft Matter Phys.* **77**, 061706 (2008).
29. H. Yoshida, Y. Tanaka, K. Kawamoto, H. Kubo, T. Tsuda, A. Fujii, S. Kuwabata, H. Kikuchi, M. Ozaki, Nanoparticle-stabilized cholesteric blue phases. *Appl. Phys. Express* **2**, 121501 (2009).
30. M. Ravnik, B. Črnko, S. Žumer, Nematic braids: Modeling of colloidal structures. *Mol. Cryst. Liq. Cryst.* **508**, 150–162 (2009).
31. H. Kikuchi, M. Yokota, Y. Hisakado, H. Yang, T. Kajiyama, Polymer-stabilized liquid crystal blue phases. *Nat. Mater.* **1**, 64–68 (2002).
32. G. Foffano, J. S. Lintuvuori, A. Tiribocchi, D. Marenduzzo, The dynamics of colloidal intrusions in liquid crystals: A simulation perspective. *Liq. Cryst. Rev.* **2**, 1–27 (2014).
33. C. Blanc, D. Coursault, E. Lacaze, Ordering nano- and microparticles assemblies with liquid crystals. *Liq. Cryst. Rev.* **1**, 83–109 (2013).
34. J. P. F. Lagerwall, G. E. Scalia, *Liquid crystals with nano and microparticles* (World Scientific, 2017), vol. 1, Series in Soft Condensed Matter, pp. 468.
35. J. P. F. Lagerwall, G. E. Scalia, *Liquid crystals with nano and microparticles* (World Scientific, 2017), vol. 2, Series in Soft Condensed Matter, pp. 440.
36. D. Pires, J.-B. Fleury, Y. Galerne, Colloid particles in the interaction field of a disclination line in a nematic phase. *Phys. Rev. Lett.* **98**, 247801 (2007).
37. X. Wang, Y.-K. Kim, E. Bukusoglu, B. Zhang, D. S. Miller, N. L. Abbott, Experimental insights into the nanostructure of the cores of topological defects in liquid crystals. *Phys. Rev. Lett.* **116**, 147801 (2016).
38. X. Wang, D. S. Miller, E. Bukusoglu, J. J. De Pablo, N. L. Abbott, Topological defects in liquid crystals as templates for molecular self-assembly. *Nat. Mater.* **15**, 106–112 (2016).
39. J. Xiang, O. D. Lavrentovich, Blue-phase-polymer-templated nematic with sub-millisecond broad-temperature range electro-optic switching. *Appl. Phys. Lett.* **103**, 051112 (2013).
40. S. Xu, Z. Nie, M. Seo, P. Lewis, E. Kumacheva, H. A. Stone, P. Garstecki, D. B. Weibel, I. Gitlin, G. M. Whitesides, Generation of monodisperse particles by using microfluidics: Control over size, shape, and composition. *Angew. Chem. Int. Ed.* **44**, 724–728 (2005).
41. B. Ren, A. Ruditskiy, J. H. Song, I. Kretzschmar, Assembly behavior of iron oxide-capped Janus particles in a magnetic field. *Langmuir* **28**, 1149–1156 (2011).
42. J. Yan, M. Bloom, S. C. Bae, E. Luijten, S. Granick, Linking synchronization to self-assembly using magnetic Janus colloids. *Nature* **491**, 578–581 (2012).
43. S. Sacanna, L. Rossi, D. J. Pine, Magnetic click colloidal assembly. *J. Am. Chem. Soc.* **134**, 6112–6115 (2012).
44. K. Han, C. W. Shields IV, N. M. Diwakar, B. Bharti, G. P. López, O. D. Velev, Sequence-encoded colloidal origami and microbot assemblies from patchy magnetic cubes. *Sci. Adv.* **3**, e1701108 (2017).
45. S. Lach, S. M. Yoon, B. A. Grzybowski, Tactic, reactive, and functional droplets outside of equilibrium. *Chem. Soc. Rev.* **45**, 4766–4796 (2016).
46. G. Villar, A. D. Graham, H. Bayley, A tissue-like printed material. *Science* **340**, 48–52 (2013).
47. Z. Yang, J. Wei, Y. I. Sobolev, B. A. Grzybowski, Systems of mechanized and reactive droplets powered by multi-responsive surfactants. *Nature* **553**, 313–318 (2018).
48. J. Fan, Y. Li, H. K. Bisoyi, R. S. Zola, D.-k. Yang, T. J. Bunning, D. A. Weitz, Q. Li, Light-directing omnidirectional circularly polarized reflection from liquid-crystal droplets. *Angew. Chem. Int. Ed.* **54**, 2160–2164 (2015).
49. C. Peng, T. Turiv, Y. Guo, S. V. Shiyanovskii, Q.-H. Wei, O. D. Lavrentovich, Control of colloidal placement by modulated molecular orientation in nematic cells. *Sci. Adv.* **2**, e1600932 (2016).

50. C. Holtze, A. C. Rowat, J. J. Agresti, J. B. Hutchison, F. E. Angilè, C. H. J. Schmitz, S. Köster, H. Duan, K. J. Humphry, R. A. Scanga, J. S. Johnson, D. Pisignano, D. A. Weitz, Biocompatible surfactants for water-in-fluorocarbon emulsions. *Lab Chip* **8**, 1632–1639 (2008).

51. R. R. Lahiji, X. Xu, R. Reifenberger, A. Raman, A. Rudie, R. J. Moon, Atomic force microscopy characterization of cellulose nanocrystals. *Langmuir* **26**, 4480–4488 (2010).

Science Advances

Nanoparticle-laden droplets of liquid crystals: Interactive morphogenesis and dynamic assembly

Yunfeng Li, Nancy Khuu, Elisabeth Prince, Moien Alizadehgiashi, Elizabeth Galati, Oleg D. Lavrentovich and Eugenia Kumacheva

ARTICLE TOOLS	http://advances.sciencemag.org/content/5/7/eaav1035
SUPPLEMENTARY MATERIALS	http://advances.sciencemag.org/content/suppl/2019/07/01/5.7.eaav1035.DC1
REFERENCES	This article cites 48 articles, 6 of which you can access for free http://advances.sciencemag.org/content/5/7/eaav1035#BIBL
PERMISSIONS	http://www.sciencemag.org/help/reprints-and-permissions

Use of this article is subject to the Terms of Service